Hindawi
International Journal of Polymer Science
Volume 2020, Article ID 3489509, 10 pages
https://doi.org/10.1155/2020/3489509

Research Article

Polypyrrole-Chitosan-$CaFe_2O_4$ Layer Sensor for Detection of Anionic and Cationic Dye Using Surface Plasmon Resonance

Amir Reza Sadrolhosseini,[1] **Pooria Moozarm Nia**,[2] **Suhaidi Shafie**,[1] **Kamyar Shameli**,[3] **and Mohd Adzir Mahdi**[4]

[1]*Functional Device Laboratory, Institute of Advanced Technology, Universiti Putra Malaysia, 43400 UPM Selangor, Malaysia*
[2]*Advance Material Research Group, Center of Hydrogen Energy, Institute of Future Energy, Universiti Teknologi Malaysia, 54100 Kuala Lumpur, Malaysia*
[3]*Malaysian-Japan International Institute of Technology, Universiti Teknologi, 541000 Kuala Lumpur, Malaysia*
[4]*Wireless and Photonics Networks Research Centre (WiPNET), Universiti Putra Malaysia, 43400 UPM Selangor, Malaysia*

Correspondence should be addressed to Amir Reza Sadrolhosseini; amir17984818@gmail.com
and Pooria Moozarm Nia; pooriamn@yahoo.com

Received 9 August 2019; Revised 1 December 2019; Accepted 6 December 2019; Published 16 January 2020

Academic Editor: Victor H. Perez

A polypyrrole-chitosan-calcium ferrite nanocomposite was prepared using the electrodeposition method. The prepared layer was characterized by using Fourier transform infrared spectroscopy, the X-ray diffraction technique, and field emission electron microscopy. The thickness of the thin layers was in the range of 2.8 nm to 59.5 nm, and the refractive index of the composite layer was in the range of $1.66131 + 0.156i$ to $1.62734 + 0.167i$. Detection and removal of cationic and anionic dyes, such as methylene blue and methylene orange, are subject of great interest for protecting environmental water. The layer composite was used to detect methylene orange and methylene blue using the surface plasmon resonance technique. Consequently, the polypyrrole-chitosan-calcium-ferrite composite layer interacted with the anionic and cationic dyes. The resonance angle shift for the detection of the cationic dye was larger than the resonance angle shift for the anionic dye. The sensor limit was achieved from a sensogram at about 0.01 ppm.

1. Introduction

Methylene orange (MO) and methylene blue (MB) are types of dye materials and they are important and major pollutants of certain industrial effluents [1]. They are highly toxic to aerobic and aquatic life, and they have carcinogenic in humans, mutagenic potential [2, 3], and neurotoxicity [4]. In the past two decades, many researchers have focused on removal and detection of dyes, such as MO and MB, from environmental areas and wastewater [1]. Many methods that are based on biological [5], chemical, and physical properties of materials [6] have been used to degrade MO and MB. The conventional methods including electrooxidation [7], electro-Fenton [8], adsorption [9], ozone [10], photocatalytic [11], and reverse osmosis [12]. The electrooxidation method is an attractive technique used to treat textile effluents [13], while decontamination of the wastewater depends on the work electrodes in electrochemical reactors [14]. Copper, zinc, platinum, and aluminum were used as cathode material [14] to degrade MO and MB using an electrooxidation technique. These techniques have limitations, however, in terms of achieving complete degradation of the dyes in wastewater or environmental areas. Therefore, a lot of materials have been used to treat wastewater including zeolite, clay, and carbon-based sorbents [15]. The nanomaterials have unique chemical and physical properties including high photocatalytic activity and nontoxicity [15]. Hence, nanoparticles were used to enhance the physical, biological, and chemical properties of absorbance composites and methods for degradation and decolorization of wastewater [16]. These nanoparticles

tend to aggregate, and they can decrease the activity [16, 17] of dyes. Silver [18], gold [19], nickel [20], iron [21], and zinc oxide [15] nanoparticles were the conventional nanoparticles used to degrade and treat the environment and wastewater. Therefore, the investigation of nanoparticles is thus a significant topic to examine to detect and degrade dye materials such as MO and MB.

Magnetic nanoparticles are an attractive class of metal and metal oxide nanoparticles. They have a large surface area, high magnetic properties, and a high adsorption rate and efficiency [22, 23]. Magnetite (Fe_3O_4) nanoparticles [23], ferrite (Fe_2O_3) nanoparticles [24], magnetite/carbon nanocomposite iron nanoparticles [25], and cobalt-zinc ferrite nanoadsorbents [26] were used to remove and purify the wastewater. Kinetic studies of them for dye adsorption fit the second-order kinetic model and Langmuir isotherm [23, 25] well. Hence, the application of magnetic nanoparticles is a connivance method for detecting and degrading pollution in an environmental area.

The surface plasmon resonance (SPR) is a versatile and high potential optical method use to consider a biosensor and sensor. The SPR is due to the interaction of light with charge density at the interface of gold layer and a dielectric medium. The SPR is an accurate method for detecting the low concentration of biomolecules and toxic chemicals. To increase the sensitivity and selectivity of the SPR sensor, the gold layer can be modified by polymer and polymer nanomaterials.

Nanomaterials such as gold, silver, zinc oxide, and magmatic nanoparticles have been used to improve the surface of gold layer to enhance the selectivity, sensitivity, and response time of the SPR sensor. Magnetic nanoparticles including $CaFe_2O_4$ NPs have superparamagnetic nature in the room temperature and they are biocompatible; hence, they have high potential to use in sensor and biosensor application and they used to detect and recognize the wide range of chemical and biochemical molecular including heavy metals, polycyclic aromatic hydrocarbons, enzymes, and tumor cells [27]. Moreover, chitosan has high compatibility with $CaFe_2O_4$ nanoparticles for sensor and degradation of toxic chemical and bimolecular [28]. Polypyrrole is a conductive polymer and it can enhance the SPR signal. Therefore, the polymer composite based on polypyrrole, chitosan, and $CaFe_2O_4$ is one of the suitable nanocomposites to improve the surface of gold layer in the SPR sensor. Hence, in this study, a polypyrrole-chitosan-$CaFe_2O_4$ NP was used to improve the surface of gold layer to detect and measure the low concentration of MO and MB using the SPR technique.

The objective of this study, therefore, is the electrochemical preparation of polypyrrole-chitosan-$CaFe_2O_4$ (PPy-Chi-$CaFe_2O_4$) to modify the gold layer to be a sensing layer that can detect MO and MB. Because the electron transfer is very slow in the polypyrrole-chitosan layer [29, 30], the magnetic nanoparticle needs to be coupled with PPy-Chi for the sensor application to increase the sensitivity of the sensor.

The detection of MO and MB is an attractive topic in the sensor field because it has an extensive application for both the environment and health care. In this current study, a polypyrrole-chitosan-$CaFe_2O_4$ thin layer was prepared using the electrodeposition technique. The prepared layer was tested using the field effect scanning electron microscopy (FE-SEM), the X-ray diffraction spectroscopy, and the Fourier transfer infrared spectroscopy (FT-IR). Thus, the characterized thin layer was used to detect MO and MB using the surface plasmon resonance technique.

2. Methodology

2.1. Reagents. Commercial, iron nitrate ($Fe(NO_3)_3{\cdot}_9H_2O$, 99%), calcium nitrate ($Ca(NO_3)_2{\cdot}6H_2O$, 99%), polyvinyl alcohol (MW = 31000 g/mol), lithium perchlorate (99%), chitosan, and potassium dihydrogen phosphate (99%) were purchased from Sigma-Aldrich Company. Methylene orange and methylene blue were provided from R&M and Systerm Companies, respectively. The reference electrode was saturated calomel electros (SCE) from BASi Company.

2.2. Preparation of MO and MB. 0.1 g of MO and MB was dissolved separately in 100 ml of the deionized distilled water (DDW) to prepare the 100 ppm solution. The high concentration of solution was systematically dissolved on the DDW to obtain the 0.01 ppm, 0.1 ppm, 1 ppm, 3 ppm, 5 ppm, 7 ppm, 10 ppm, and 20 ppm.

2.3. Preparation of PPy-Chi-$CaFe_2O_4$ Composite Layer

2.3.1. Synthesis of $CaFe_2O_4$. Priority to synthesize a PPy-Chi-$CaFe_2O_4$ nanocomposite layer, PVA/$CaFe_2O_4$ nanocomposite was synthesized using the thermal treatment method [31–33]. $Ca(NO_3)_2{\cdot}H_2O$, $Fe(NO_3)_3{\cdot}H_2O$, DDW, and polyvinyl alcohol (PVA) were used to precursors, solvent, and capping agent, respectively [31].

3.5 g of PVA was dissolved in 100 ml of DDW at 353. After that, 0.2 mmol $Fe(NO_3)_3{\cdot}H_2O$ and 0.1 mmol $Ca(NO_3)_2{\cdot}H_2$ (Fe : Ca = 2 : 1) were added into the PVA solution and the mixture was stirred constantly for 1.5 h, and a clear solution was obtained. The clear mixture was heated at 362 K for 24 h to remove the solvent (DDW) and the solid $CaFe_2O_4$ was reminded. The product was grounded in a mortar to obtain the uniform powder and it was heated at 830 K for crystallization of nanocrystal and decomposition of the PVA. Final powder was used to prepare the PPy-Chi-$CaFe_2O_4$.

2.3.2. Synthesis of PPy-Chi-$CaFe_2O_4$ Composite Layer. The electropolymerization of the polypyrrole-chitosan-$CaFe_2O_4$ on the surface of the gold coated glass slide (gold/PPy-Chi-Fe_2O_4) was carried out using the amperometry method. The monomer solution contains mixed electrolytes in a 0.1 M phosphate-buffered solution (pH 7.2), 0.1 M pyrrole monomer, 0.1 M $LiClO_4$ as a dopant, 0.1 M chitosan, and 0.05 grams of the $CaFe_2O_4$. The electrolyte was stirred during electrodeposition to make sure there is no precipitation. The working electrode, reference electrode, and counter electrode were gold-coated glass slide, saturated calomel electros (SCE), and platinum electrode, respectively. The polymerization of pyrrole was carried out at the constant potential of 0.8 V in the presence of chitosan and $CaFe_2O_4$ nanoparticles at the different times in the range of 20 s to 1000 s. The prepared samples were put in the oven for 2 h to dry layer. The PPy-Chi-$CaFe_2O_4$ composite layers were characterized

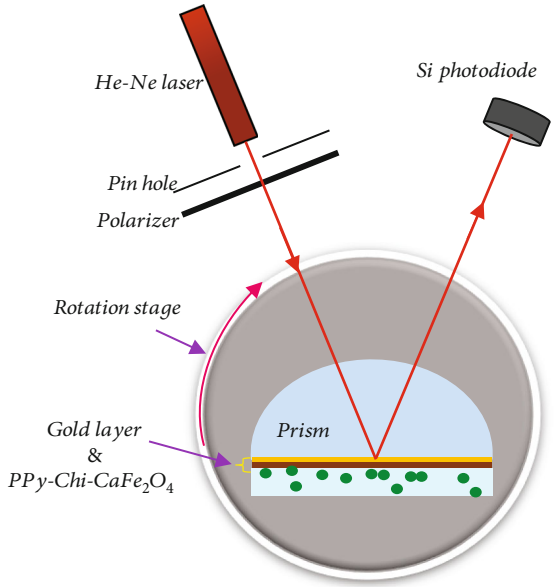

Figure 1: SPR setup contains a high index prism, a He-Ne laser (632.8 nm, model: R30990, Newport), a pinhole, a chopper, a polarizer, and a silicon photodetector [34–36].

using the Fourier transform infrared spectroscopy (FT-IR; model: NEXUS), the X-ray diffraction spectroscopy (XRD; WITec, Alpha 300R with Shimadzu diffractometer: model XRD6000 and Cu, Ka (0.154 nm)), and the field effect scanning electron microscopy (FE-SEM; NOVA NANOSEM 230), and the chemical elements were evaluated using the energy-dispersive spectroscopy (EDX) from Oxford Instruments (X-Max).

2.4. SPR Setup. The SPR setup based on the Kretschmann configuration with prism coupling was used to measure the low concentration of MO and MB. Figure 1 shows the homemade SPR setup based on angular modulation and the laser beam intensity was registered using photodetector and a lock-in amplifier (Stanford Research) at different angles.

The gold layer was modified using the PPy-Chi-$CaFe_2O_4$ nanocomposite layer (sensing layer). The gold layer/PPy-Chi-$CaFe_2O_4$ layer was coated on the glass slide which was attached to a high index prism (SF52, Foctek) using index matching gel (F-IMF-105, Newport, USA) [34, 35]. The prism was placed on a precision rotation stage, and the sample tank was attached to prism and sensing layer. MO and MB were flowed separately into the tank to interact with sensing layer. The prism was rotated up to 20° at increments of a 0.1°. The polarizer provided the TM mode and the surface plasmon wave was exited. Hence, the intensity of laser beam changed due to rotation of prism. The variation of laser beam intensity with the angle was registered, when the prism was stopped momentarily.

The experiment was repeated separately for each sample about 10 times. SPR signal was analyzed using Fresnel's theory based on the matrix method for a multilayer system [36–38].

Fresnel's theory in the matrix form for multilayer was used [39] to analyze SPR signal using computer program. The root square method was considered to find the resonance angle as follows:

$$\Omega = \sum \left| \left(R_{\mathrm{Th}}\left(\theta, n_g, n_a, n_{sl}, t_g, t_{sl}\right) - R_{\mathrm{Exp}}\left(\theta, n_g, n_a, n_{sl}, t_g, t_{sl}\right)\right)\right|, \tag{1}$$

where R_{Th} and R_{Exp} are the computed reflectivity from Fresnel's theory and the experimental reflectivity, respectively. θ, n_g, n_a, n_{sl}, t_g, and t_{sl} are the resonance angle, refractive index of gold layer, analyte (water or solvent), sensing layer, thicknesses of sensing layer, and gold layer, respectively. The SPR signal was analyzed based on Fresnel's theory related to the parallel N layers.

As a literature, the SPR signal was obtained, when the transverse magnetic mode (TM) interacts with the metal layer and it occurred at the interface of medium with opposite dialectic sign. Therefore, the reflection coefficient of TM mode is as follows:

$$r = -\frac{v_0 - w}{v_0 + w}, \tag{2}$$

where v_0 and w are the admittance of layer and multilayer system for TM mode of laser beam. w was derived from multiplication of matrix of each layer as follows:

$$\begin{pmatrix} 1 \\ w \end{pmatrix} = \left(\prod_{j=1}^{N} \begin{vmatrix} \cos\delta_j & \left(\frac{i}{v_j}\right)\sin\delta_j \\ iv_j \sin\delta_j & \cos\delta_j \end{vmatrix} \right) \begin{pmatrix} 1 \\ v_N \end{pmatrix}, \tag{3}$$

$$\delta_j = 2\pi n_i \frac{t_j}{\lambda} \cos\varphi_j, \tag{4}$$

where δ_j, n_i, t_j, λ, and φ_j are phase, refractive index of n^{th} layer, thickness of layer, wavelength, and angle of incidence, respectively.

An admittance (v_j) of j^{th} layer is defined as follows:

$$v_j = \frac{n_j^2}{\sqrt{n_j^2 - n_j^2 \sin^2\varphi_0}}. \tag{5}$$

The refractive index of j^{th} layer is $n_j = n_{Rj} - ik_{Ij}$ (n_{Rj} and k_{Ij} are the real and imaginary parts of layer), and the reflectivity is $R = r \times r$ [39–41].

3. Results and Discussion

Figures 2(a)–2(d) show the FT-IR spectrum, the XRD spectrum, the FE-SEM image, and the EDX analysis.

The main peaks of the FT-IR spectrum appeared at 3271.47, 2931.3, 1625.50, 1517.50, 1415.11, 1274.58, 998.75, 657.38, and 609.68 cm^{-1}. The peaks at 3271.47, 1517.50, and 1415.11 cm^{-1} correspond to the stretching vibrations of N-H, C-N, and C-C in the pyrrole ring, respectively [42, 43].

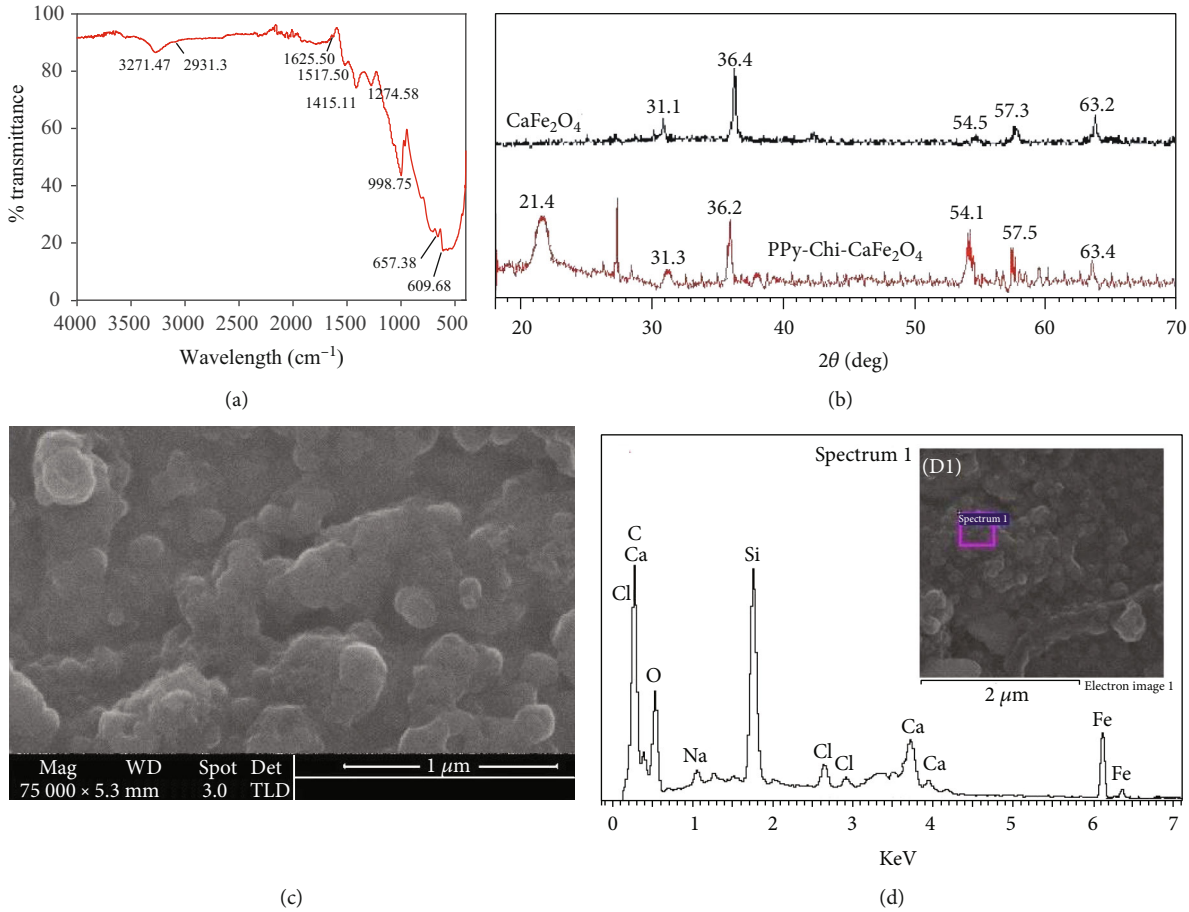

Figure 2: (a) The FT-IR spectrum, (b) the XRD spectrum, (c) the HR-TEM image, and (d) the EDX analysis of the PPy-Chi-$CaFe_2O_4$ as sensing layer.

The peak centered at 2931.3 cm^{-1} was assigned to the asymmetric vibration of CH_2, and the peaks that appeared at 1274.58 and 998.75 cm^{-1} were related to the typical C-H deformation and the C-N stretching vibration of PPy, respectively. Moreover, the peaks located at 3271.47 and 2931.3 cm^{-1} corresponded to N-H while the vibration of CH_2 of the chitosan chain overlapped on the vibration of N=H and CH_2 in polypyrrole [43]. The peaks at 1625.50, 657.38, and 609.68 cm^{-1} presented a vibration of C=O in the amid band, N-H out of plane, and O-H out of plan in chitosan [41].

Figure 2(b) depicts the XRD pattern of the $CaFe_2O_4$-NPs powder and the PPy-Chi-$CaFe_2O_4$ composite layer. In accordance with the literature, the XRD spectrum of PPy-Chi shows a broad peak at 21.4° [44] that explains the PPy-Chi formed in the amorphous form in the thin layer. The XRD pattern of $CaFe_2O_4$ displays the main peak at 31.1°, 36.4°, 57.3°, 54.5°, and 63.2° which confirm that $CaFe_2O_4$ has a cubic structure [31]. The XRD pattern of PPy-Chi-$CaFe_2O_4$ shows its peak at 21.5°, and new peaks at 31.3°, 36.2°, 57.5°, 54.1°, and 63.4° which confirm that $CaFe_2O_4$ also formed in the composite layer in the cubic structure.

Figures 2(c) and 2(d) show the FE-SEM images and the EDX spectrum of PPy-Chi-$CaFe_2O_4$, respectively. As a result, the chitosan agglomerated the polypyrrole during the electropolymerization of pyrrole and the $CaFe_2O_4$ increased both the agglomeration and coagulation process of pyrrole in the formation of the PPy-Chi-$CaFe_2O_4$ composite layer. $CaFe_2O_4$-NPs impressed the morphology of the PPy-Chi-$CaFe_2O_4$ composite layer, and it was scattered on the surface of layer. Figure 2(d) shows the EDX spectrum for the PPy-Chi-$CaFe_2O_4$ composite layer.

The main peaks appeared at 0.3, 3.7, 3.95, 6.2, and 6.45 keV. The peaks at 0.3, 3.7, and 3.95 keV corresponded to Ca while the peaks at 6.4 and 6.45 keV were assigned to Fe. Moreover, the EDX spectrum shows peaks at 0.27, 0.5, 1.1, 2.7, and 2.9 keV that related to C, O, Na, and Cl, respectively [31]. The weight % values of Cl, Na, C, and O were 1.27, 0.73, 23.44, and 22.4%, respectively. The contributions of Fe and Ca to the total weight percentage were 17.81% and 34.3%, respectively.

The different thicknesses of PPy-Chi-$CaFe_2O_4$ were considered to find the refractive index of the sensing layer. The PPy-Chi-$CaFe_2O_4$ composite layer was coated on the surface of the gold layer. The system of gold/PPy-Chi-$CaFe_2O_4$ composite layer was attached to the prism and the DDW ($n = 1.3322$) as it flowed in to the sample container that contacted the high index prism. The thickness of the gold layer was 49.5 nm, and the thickness of the sensing layer measured using a profilometer (AMBIOS, XP-200) was in the range of 2.8 nm to 59.5 nm, the refractive index of the gold layer was

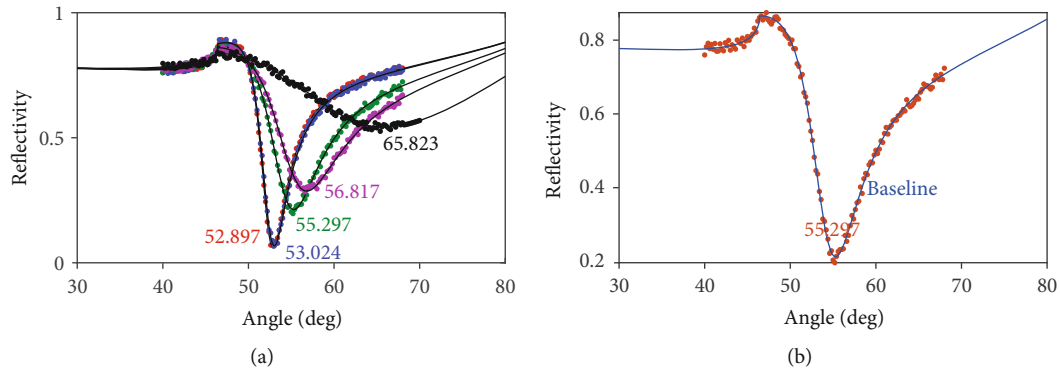

Figure 3: (a) The SPR signals corresponding to different thicknesses of layer. The resonance angle was in the range of 52.897° to 65.823°. (b) The SPR signal to determine the baseline (55.297°) for using the detection of MO and MB.

Table 1: The resonance angle and the refractive index of layer.

Sample	Electrodeposition time (s)	Thickness (nm)	Refractive index	Resonance angle (deg)
1	10	2.8	1.66131 + 0.156i	52.897
2	20	3.4	1.65842 + 0.157i	53.024
3	420	13.6	1.63421 + 0.161i	55.297
4	500	19.8	1.63031 + 0.163i	56.817
5	1000	59.5	1.62734 + 0.167i	65.823

0.236 + 3.34i. The SPR signals of each layer, as presented in Figure 3(a), were registered using a homemade SPR setup. The SPR signals were analyzed using Fresnel's equations (Equations (1), (2) and (3)) to find the refractive index of the PPy-Chi-$CaFe_2O_4$ composite layer. The thickness of the layers, the refractive index of the layers, and the resonance angle of each layer are listed in Table 1. The refractive index of the layers was ranged from 1.66131 + 0.156i to 1.62734 + 0.167i. When the thickness of a layer increased, the real part of the refractive index decreased, while the imaginary part of the refractive index increased. The variation in the real and imaginary parts was opposite to each other and was explained using the Kramers–Kronig formula [33, 45]. The SPR signal was achieved in the 13.6 nm thickness and used as a baseline. Figure 3(b) depicts the baseline, which was achieved at 55.297° when the resonance angle was obtained for the PPy-Chi-$CaFe_2O_4$ composite layer in the presence of DDW and without any impurities (MO and MB).

The MO and MB solutions in concentrations of 0.01, 0.1, 5, 10, and 20 ppm were separately put in contact to PPy-Chi-$CaFe_2O_4$ via a sample tank. The variation in the resonance angle was registered during the 420 s for different concentrations of MO and MB. Figures 4(a) and 4(b) show the variation in the resonance angle shift over time (sensogram) for MO and MB, respectively. As a result, the resonance angle shift increased when the concentration of MO and MB was increased. The minimum variation of the resonance angle shift was achieved with a 0.01 ppm concentration of MO and MB, and the saturation value ($\Delta\theta_{Sat}$) occurred after 350 seconds. The value of the resonance angle shift at 420 seconds was considered to obtain the variation of the resonance angle shift with a concentration of MO and MB. Figure 4(c) depicts the variation in the resonance angle shift with different concentrations of MO and MB. The doted points are the experimental value of resonance angle shift and the value of the resonance angle shift at the saturation ($\Delta\theta_{Sat}$) part, respectively, and solid lines are Langmuir's formula as follows [26, 41, 46]:

$$\Delta\theta_{Sat} = \frac{\Delta\theta_{max} \times C \times K}{1 + K \times C}, \quad (6)$$

where $\Delta\theta_{max}$, C, and K are the resonance angle shift at the maximum value, the concentration of analyte, and the affinity constant, respectively. The affinity constants for MO and MB were about 2.138 and 4.483, respectively. These results authenticated that the experimental value fit Langmuir's theory well. Figure 4(c) shows that the variation in the resonance angle shift for different concentrations of MB is larger than the variation of resonance angle shift for different concentrations of MO and confirms that the binding and interaction of MB with the sensing layer is stronger than the interaction of MO with the PPy-Chi-$CaFe_2O_4$ composite layer.

The concentration of MO and MB was measured for 1 ppm using the UV-vis spectrum. The MO and MB in 1 ppm were separately put in the contact with the sensing layer and the concentration of samples was measured before and after the interaction of the sensing layer with MO and MB. Figures 5(a) and 5(b) show the UV-Vis spectra for MO and MB in 1 ppm, 3 ppm, 5 ppm, and 7 ppm as standard

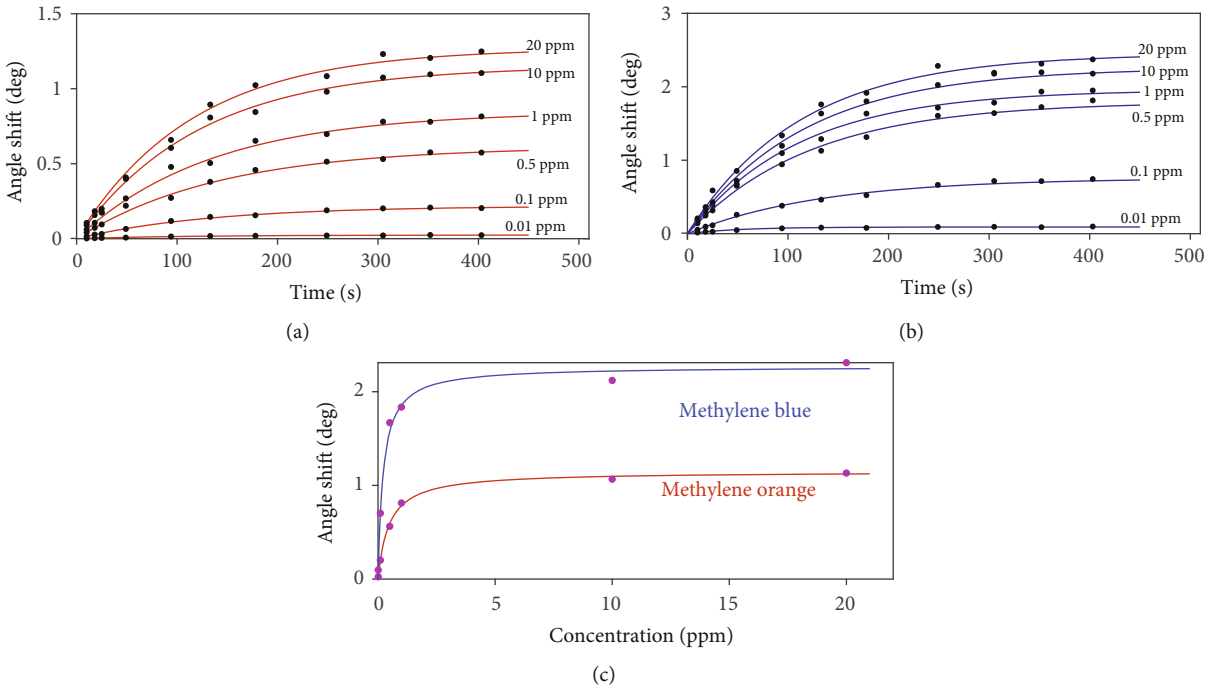

Figure 4: Variation of the resonance angle shift with time for (a) MO and (b) MB. (c) Variation of the resonance angle shift with different concentrations of MO and MB. The solid lines in parts (a) and (b) fit first-order Langmuir theory well.

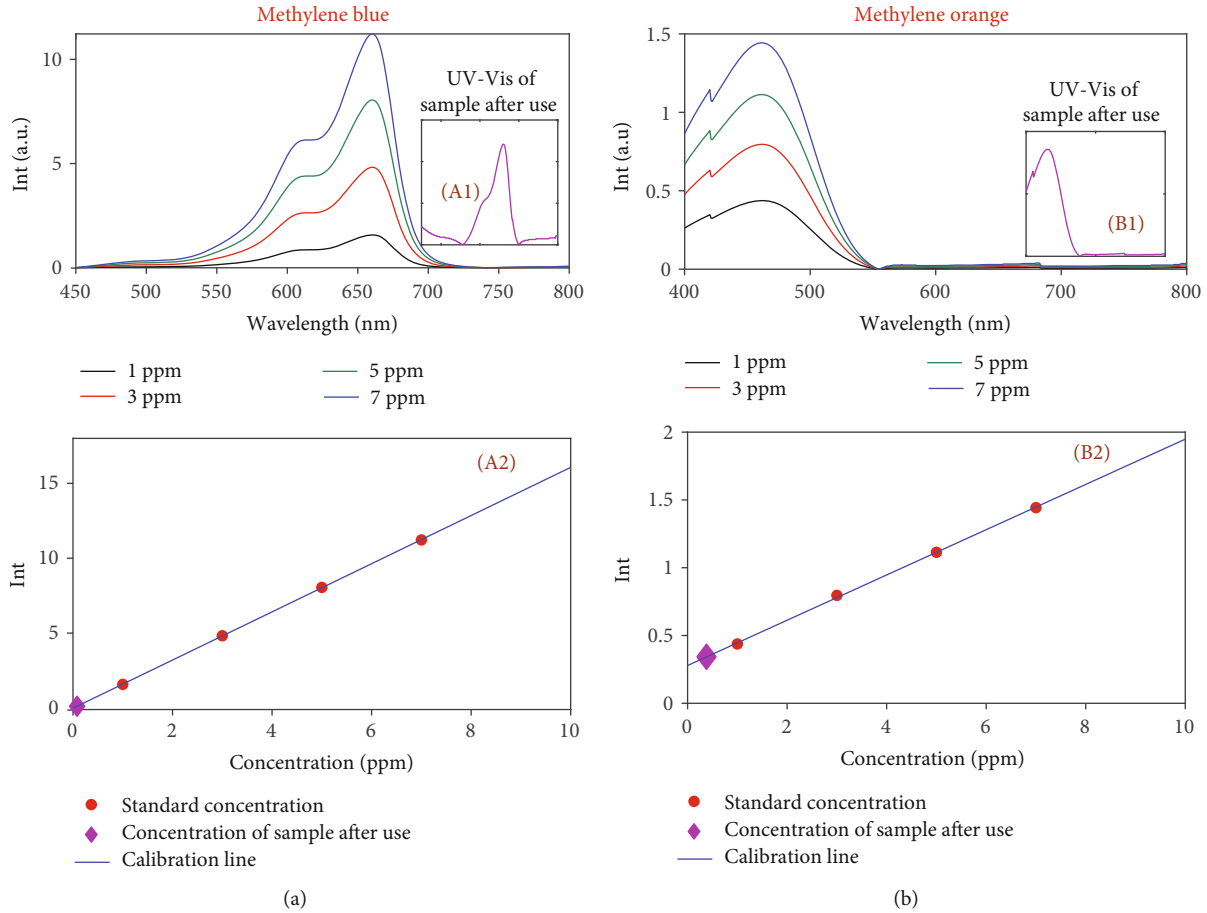

Figure 5: The UV-Vis spectra of (a) MB and (b) MO. The UV-Vis spectra of (a1) MB and (b1) MO after interaction with the sensing layer. The calibration curve for (a2) MB and (b2) MO.

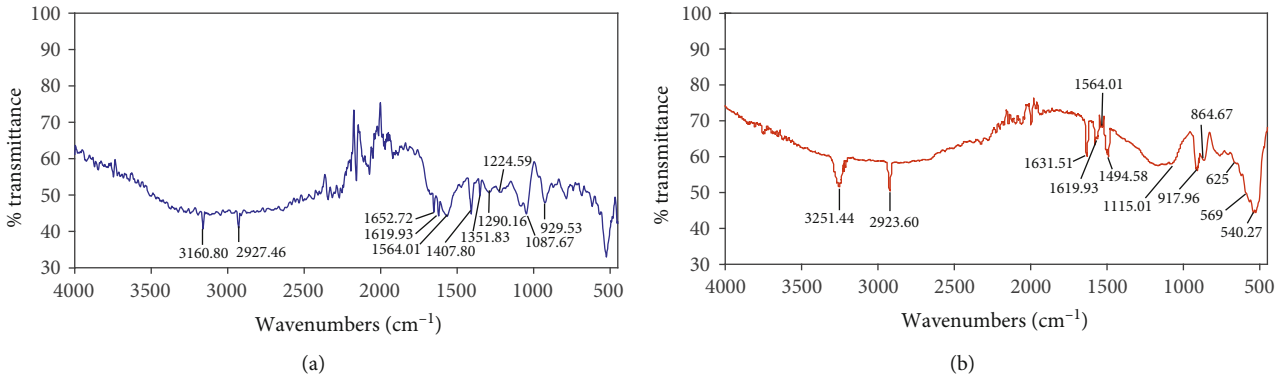

Figure 6: The FT-IR results related to PPy-Chi-$CaFe_2O_4$ sensing layer after the interaction with (a) MB and (b) MO.

samples. The calibration curves are derived in Figures 5(A2) and 5(B2) for MB and MO, respectively. Figures 5(A1) and 5(B1) depict the UV-Vis spectra for MB and MO solutions after the interaction with the sensing layer. As a result, the concentrations of MB and MO were 0.082 ppm and 0.38 ppm.

If the C_0 and C_f were the initial and final concentrations of samples, respectively, the degree of sensing layer absorption for MB and MO was estimated using $E = 100(C_0 - C_f)/C_0$ [33, 47, 48]. Therefore, the degree of absorption [49, 50] for MB and MO was achieved at 91.8% and 62%, respectively. Consequently, MB has a higher tendency to interact with the PPy-Chi-$CaFe_2O_4$ composite layer.

Figure 6(a) shows the FT-IR result after the experiment and contact Mb with the PPy-Chi-$CaFe_2O_4$ sensing layer. The main peaks appeared at 3160.80, 2927.46, 1652.72, 1619.93, 1564.01, 1407.80, 1351.83, 1224.59, 1290.16, 1087.67, and 929.53 cm^{-1}. The peaks at 1652.72, 1351.83, 1224.59, 1087.67, and 929.53 cm^{-1} corresponded to the C-N$^+$(CH$_3$)$_2$ stretching vibrations [34], stretching vibration of the C-N [34], C-H bond vibrations [34], C-S-C vibration [35] of MB, and bound vibration of C-H in MB [51], respectively. The peak occurred at 1564.01 cm^{-1} is related to C=N and C=C vibration of MB [34]. The peak at 1407.80 cm^{-1} assigned the aromatic ring vibration in MB. Consequently, these peaks authenticated the interaction of MB with sensing layer. The peaks at 3160.80, 2927.46, 1619.93, and 1290.16 cm^{-1} related to functional group of PPy-Chi-$CaFe_2O_4$ composite layer. If these peaks are compared with the main peaks which were appeared in Figure 2(a), it obtains that the main peaks in the FT-IR spectrum (Figure 6(a)) have a shift after the interaction of the PPy-Chi-$CaFe_2O_4$ sensing layer with MB.

Figure 6(b) depicts the FT-IR spectrum of PPy-Chi-$CaFe_2O_4$ sensing layer after interaction with MO. The peaks at 3251.44 and 2923.6 cm^{-1} related to PPy and Chi. The peaks at 3251.44 and 2923.60 cm^{-1} assigned the N-H stretching vibration and C-H stretching vibration in MO and chitosan that overlapped to gather. The peaks at 1619.93, 1494.58, 917.96, 625, 569, and 540 cm^{-1} corresponded to functional groups of PPy-Chi-$CaFe_2O_4$ composite layer. If these peaks are compared with the similar peaks in Figure 2(a), it obtains that the peaks have a shift. The peaks at 1631.51, 1564.01, 1115.01, and 864.67 cm^{-1} related to C=C stretching vibration, –C=C stretching vibration, -S=O stretching vibration, and -C-H bending vibration, in MO [52]. Consequently, the FT-IR spectrum contains the main peaks of PPy-Chi-$CaFe_2O_4$ composite layer and MO, and it confirms the interaction of MO with sensing layer.

Figure 7 shows the mechanism for the interaction and binding of MB and MO with the PPy-Chi-$CaFe_2O_4$ composite layer. This binding is based on the electrostatic interaction of delocalized electrons of the PPy-Chi-$CaFe_2O_4$ composite layer with MB and MO.

The PPy-Chi-$CaFe_2O_4$ composite layer was synthesized on the surface of the gold thin layer using electropolymerization of the pyrrole. The chitosan and $CaFe_2O_4$-NPs were presented during the formation of that PPy-Chi-$CaFe_2O_4$ composite layer in the solution.

The main components that were attracted and interacted with the MO and MB were $CaFe_2O_4$-NPs and chitosan by transfer electron. Poly(b-1-4)-2-amino-2-deoxy-D-glucopyranose is chitosan, and it was achieved from chitin by a full alkaline N-deactylation of the main chitin. The hydroxyl and amino $(-NH_2)^+$ tail groups of the chitosan interacted with MO and MB, [48, 53, 54]. Moreover, the MB placed a positive electrical charge on the $(-NH_2)^+$ tail [48] which has a tendency to interact with $CaFe_2O_4$-NPs. Hence, the $CaFe_2O_4$, the amino group of chitosan, are the essential component and functional group that are implicated in binding MO and MB to the sensing layer. MO has a negative charge density on the $(-SO_3Na)^-$ [48] and was immobilized on the chitosan via the amino group in the square plan of the chitosan molecule structure, and MB was absorbed and immobilized via $CaFe_2O_4$-NPs (see Figure 7) and the hydroxyl group in the plan for the chitosan structure [55, 56]. Accordingly, the PPy-Chi-$CaFe_2O_4$ nanocomposite sensing layer has a strong interaction with MB. Consequently, as seen in Figure 4, the resonance angle shift to detect MB is larger than the resonance angle shift and the response of the sensing layer to detect MO.

4. Conclusion

The PPy-Chi-$CaFe_2O_4$ composite layer was prepared in different thicknesses in the range of 2.8 nm to 59.5 nm using

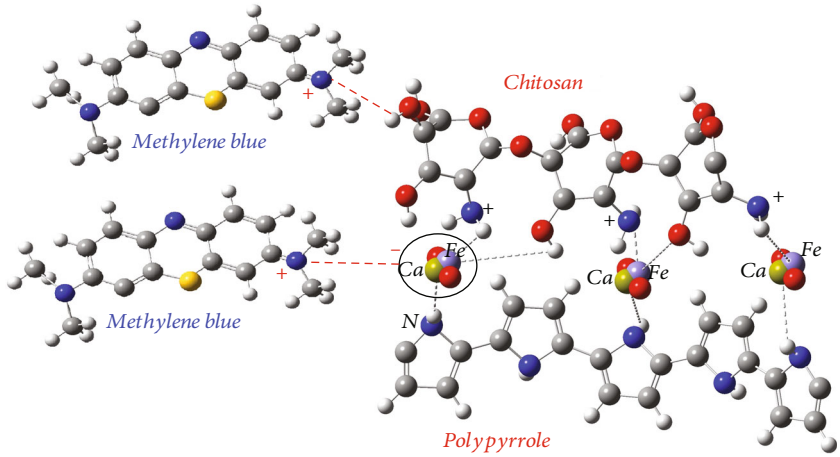

Figure 7: Molecular structure of PPy-Chi-$CaFe_2O_4$ and interaction of methylene blue with it.

the electrodeposition technique. The composite layer was characterized with analytical methods including the FT-IR, FE-SEM, and XRD techniques, and they confirmed the $CaFe_2O_4$ was formed in the polypyrrole and chitosan composite. The refractive index of each layer was measured using the SPR technique prior to them use for detection of MO and MB. Therefore, the refractive indies were in the range of $1.66131 + 0.156i$ to $1.62734 + 0.167i$. The thickness and imaginary part of the composite layer increased by increasing the electrodeposition time while the real part of refractive index decreased when the thickness of the layer increased. The SPR experiment was carried out to detect the MO and MB in aqueous solutions for concentration of 0.01, 0.1, 0.5, 1, 10, and 20 ppm. The variation of resonance angle with time and the variation of resonance angle with concentrations of MO and MB were achieved, and the experimental results fitted with Langmuir's theory. Consequently, the resonance angle shift increased in the presence of MO and MB, and the limit sensor was about 0.01 ppm. The variation in the resonance angle shift for MB was larger than the variation of resonance angle shift for MO. The FT-IR spectra of sensing layer after the sensing of MO and MB using PPy-Chi-$CaFe_2O_4$ composite layer confirmed the MO and MB were interacted with sensing layer. Consequently, the PPy-Chi-$CaFe_2O_4$ nonconposite layer can detect the cationic and anionic dyes, while the sensitivity of the PPy-Chi-$CaFe_2O_4$ thin layer to detect MB is higher than sensitivity for MO.

Data Availability

The data used to support the findings of this study are available from the corresponding author upon request.

Conflicts of Interest

The authors declare that there are no conflicts of interest regarding the publication of this paper.

Acknowledgments

The authors acknowledge funding from the Universiti Putra Malaysia, under Geran Putra Berimpak (UPM/800-3/3/1/GPB/2019/9674700) and Institute of Advanced Technology (ITMA) UPM for providing the analytical facilities.

References

[1] C.-T. Wang, W.-L. Chou, Y.-M. Kuo, and F.-L. Chang, "Paired removal of color and COD from textile dyeing wastewater by simultaneous anodic and indirect cathodic oxidation," *Journal of Hazardous Materials*, vol. 169, no. 1-3, pp. 16–22, 2009.

[2] S. Srivastava, R. Sinha, and D. Roy, "Toxicological effects of malachite green," *Aquatic Toxicology*, vol. 66, no. 3, pp. 319–329, 2004.

[3] P. A. Soloman, C. A. Basha, M. Velan, and B. Subramanian, "Electro oxidation of malachite green and modeling using ANN," *Chemical and Biochemical Engineering Quarterly*, vol. 24, pp. 445–452, 2010.

[4] Y. Alici-Evcimen and W. S. Breitbart, "Ifosfamide neuropsychiatric toxicity in patients with cancer," *Psycho-Oncology*, vol. 16, no. 10, pp. 956–960, 2007.

[5] X. Xia, Z. Zhou, S. Wu, D. Wang, S. Zheng, and G. Wang, "Adsorption removal of multiple dyes using biogenic selenium nanoparticles from an *Escherichia coli* strain overexpressed selenite reductase CsrF," *Nanomaterials*, vol. 8, no. 4, p. 234, 2018.

[6] T. Robinson, G. McMullan, R. Marchant, and P. Nigam, "Remediation of dyes in textile effluent: a critical review on current treatment technologies with a proposed alternative," *Bioresource Technology*, vol. 77, no. 3, pp. 247–255, 2001.

[7] J. B. Parsa and R. Shojaat, "Removal of organic dye pollutants from wastewater by electrochemical oxidation," *Physics and Chemistry of Liquids*, vol. 45, no. 4, pp. 479–485, 2007.

[8] C.-T. Wang, J.-L. Hu, W.-L. Chou, and Y.-M. Kuo, "Removal of color from real dyeing wastewater by electro-Fenton technology using a three-dimensional graphite cathode," *Journal of Hazardous Materials*, vol. 152, no. 2, pp. 601–606, 2008.

[9] B. A. Fil, C. Özmetin, and M. Korkmaz, "Cationic dye (methylene blue) removal from aqueous solution by

montmorillonite," *Bulletin of the Korean Chemical Society*, vol. 33, no. 10, pp. 3184–3190, 2012.

[10] M. F. Sevimli and H. Z. Sarikaya, "Ozone treatment of textile effluents and dyes: effect of applied ozone dose, pH and dye concentration," *Journal of Chemical Technology and Biotechnology*, vol. 77, no. 7, pp. 842–850, 2002.

[11] J. Shen, Y. N. Wu, L. Fu, B. Zhang, and F. Li, "Preparation of doped TiO_2 nanofiber membranes through electrospinning and their application for photocatalytic degradation of malachite green," *Journal of Materials Science*, vol. 49, no. 5, pp. 2303–2314, 2014.

[12] M. F. Abid, M. A. Zablouk, and A. M. Abid-Alameer, "Experimental study of dye removal from industrial wastewater by membrane technologies of reverse osmosis and nanofiltration," *Iranian Journal of Environmental Health Science & Engineering*, vol. 9, no. 1, pp. 1–9, 2012.

[13] B. Farizoğlu et al., "Reactive black 5 removal with electrooxidation method using $Ti/IrO_2/RuO_2$ anode and stainless steel cathode," *International Journal of Electrochemical Science*, vol. 13, pp. 3288–3296, 2018.

[14] A. N. S. Rao and V. T. Venkatarangaiah, "The effect of cathode materials on indirect electrochemical oxidation of methyl orange, malachite green and methylene blue," *Portugaliae Electrochimica Acta*, vol. 32, no. 3, pp. 213–231, 2014.

[15] Z. M. Khoshhesab and S. Souhani, "Adsorptive removal of reactive dyes from aqueous solutions using zinc oxide nanoparticles," *Journal of the Chinese Chemical Society*, vol. 65, no. 12, pp. 1482–1490, 2018.

[16] R. D. Kale and P. B. Kane, "Colour removal using nanoparticles," *Textiles and Clothing Sustainability*, vol. 2, no. 1, p. 4, 2017.

[17] N. Toshima, "Capped bimetallic and trimetallic nanoparticles for catalysis and information technology," *Macromolecular Symposia*, vol. 270, no. 1, pp. 27–39, 2008.

[18] N. Khatoon and M. Sardar, "Efficient removal of toxic textile dyes using silver nanocomposites," *Journal of Nanosciences: Current Research*, vol. 2, p. 3, 2017.

[19] Z. A. Tagar, M. N. Sirajuddin, N. Memon et al., "Facile synthesis, characterization and catalytic function of gelatin stabilized gold nanoparticles," *Pakistan Journal of Analytical & Environmental Chemistry*, vol. 13, pp. 70–77, 2012.

[20] N. H. Kalwar et al., "Fabrication of small l-threonine capped nickel nanoparticles and their catalytic application," *Applied Catalysis A: General*, vol. 453, pp. 54–59, 2013.

[21] N. Ahuja, A. K. Chopra, and A. A. Ansari, "Removal of colour from aqueous solutions by using zero valent iron nanoparticles," *IOSR Journal of Environmental Science, Toxicology and Food Technology*, vol. 10, pp. 4–14, 2016.

[22] L. C. A. Oliveira, R. V. R. A. Rios, J. D. Fabris, K. Sapag, V. K. Garg, and R. M. Lago, "Clay-iron oxide magnetic composites for the adsorption of contaminants in water," *Applied Clay Science*, vol. 22, no. 4, pp. 169–177, 2003.

[23] F. Keyhanian, S. Shariati, M. Faraji, and M. Hesabi, "Magnetite nanoparticles with surface modification for removal of methyl violet from aqueous solutions," *Arabian Journal of Chemistry*, vol. 9, pp. S348–S354, 2016.

[24] N. M. Mahmoodi, J. Abdi, and D. Bastani, "Direct dyes removal using modified magnetic ferrite nanoparticle," *Journal of Environmental Health Science and Engineering*, vol. 12, no. 1, p. 96, 2014.

[25] S. G. Muntean, M. A. Nistor, E. Muntean, A. Todea, R. Ianoş, and C. Păcurariu, "Removal of colored organic pollutants from wastewaters by magnetite/carbon nanocomposites: single and binary systems," *Journal of Chemistry*, vol. 2018, Article ID 6249821, 16 pages, 2018.

[26] T. Tatarchuk, N. Paliychuk, R. B. Bitra et al., "Adsorptive removal of toxic methylene blue and acid orange 7 dyes from aqueous medium using cobalt-zinc ferrite nanoadsorbents," *Desalination and Water Treatment*, vol. 150, pp. 374–385, 2019.

[27] A. Manohar and C. Krishnamoorthi, "Structural, optical, dielectric and magnetic properties of $CaFe_2O_4$ nanocrystals prepared by solvothermal reflux method," *Journal of Alloys and Compounds*, vol. 722, pp. 818–827, 2017.

[28] R. Bilas, K. Sriram, P. Maheswari, and K. Sheriffa Begum, "Highly biocompatible chitosan with super paramagnetic calcium ferrite ($CaFe_2O_4$) nanoparticle for the release of ampicillin," *International Journal of Biological Macromolecules*, vol. 97, pp. 513–525, 2017.

[29] Z. He, R. V. Gudavarthy, J. A. Koza, and J. A. Switzer, "Room-temperature Electrochemical reduction of epitaxial magnetite films to epitaxial iron films," *Journal of the American Chemical Society*, vol. 133, no. 32, pp. 12358–12361, 2011.

[30] A. M. A. Abdul, A. al-Mokaram, R. Yahya, M. M. Abdi, and H. N. M. E. Mahmud, "One-step electrochemical deposition of Polypyrrole-Chitosan-Iron oxide nanocomposite films for non-enzymatic glucose biosensor," *Materials Letters*, vol. 183, pp. 90–93, 2016.

[31] M. Naseri, E. Naderi, and A. R. Sadrolhosseini, "Effect of phase transformation on physical and biological properties of PVA/-$CaFe_2O_4$ nanocomposite," *Fibers and Polymers*, vol. 17, no. 10, pp. 1667–1674, 2016.

[32] M. G. Naseri, E. B. Saion, H. A. Ahangar, M. Hashim, and A. H. Shaari, "Simple preparation and characterization of nickel ferrite nanocrystals by a thermal treatment method," *Powder Technology*, vol. 212, no. 1, pp. 80–88, 2011.

[33] A. R. Sadrolhosseini, M. Naseri, and S. A. Rashid, "Polypyrrole-chitosan/nickel-ferrite nanoparticle composite layer for detecting heavy metal ions using surface plasmon resonance technique," *Optics and Laser Technology*, vol. 93, pp. 216–223, 2017.

[34] A. Bartošová, L. Blinová, M. Sirotiak, and A. Michalíková, "Usage of FTIR-ATR as non-destructive analysis of selected toxic dyes," *Research Papers Faculty of Materials Science and Technology Slovak University of Technology*, vol. 25, no. 40, pp. 103–111, 2017.

[35] O. V. Ovchinnikov, A. V. Evtukhova, T. S. Kondratenko, M. S. Smirnov, V. Y. Khokhlov, and O. V. Erina, "Manifestation of intermolecular interactions in FTIR spectra of methylene blue molecules," *Vibrational Spectroscopy*, vol. 86, pp. 181–189, 2016.

[36] A. R. Sadrolhosseini, M. Naseri, and H. M. Kamari, "Surface plasmon resonance sensor for detecting of arsenic in aqueous solution using polypyrrole-chitosan-cobalt ferrite nanoparticles composite layer," *Optics Communications*, vol. 383, pp. 132–137, 2017.

[37] A. R. Sadrolhosseini, S. A. Rashid, N. Jamaludin, A. S. M. Noor, and A. M. Isloor, "Surface plasmon resonance sensor using polypyrrole-chitosan/graphene quantum dots layer for detection of sugar," *Materials Research Express*, vol. 6, no. 7, article 075028, 2019.

[38] G. Xia, C. Zhou, S. Jin, C. Huang, J. Xing, and Z. Liu, "Sensitivity enhancement of two-dimensional materials based on genetic optimization in surface plasmon resonance," *Sensors*, vol. 19, no. 5, p. 1198, 2019.

[39] A. R. Sadrolhosseini, A. S. M. Noor, M. M. Moksin, M. M. Abdi, and A. Mohammadi, "Application of polypyrrole-chitosan layer for detection of Zn (II) and Ni (II) in aqueous solutions using surface plasmon resonance," *International Journal of Polymeric Materials and Polymeric Biomaterials*, vol. 62, no. 5, pp. 284–287, 2013.

[40] R. Bassi, S. O. Prasher, and B. K. Simpson, "Removal of selected metal ions from aqueous solutions using chitosan flakes," *Separation Science and Technology*, vol. 35, no. 4, pp. 547–560, 2000.

[41] G. V. Beketov, Y. M. Shirshov, O. V. Shynkarenko, and V. I. Chegel, "Surface plasmon resonance spectroscopy: prospects of superstrate refractive index variation for separate extraction of molecular layer parameters," *Sensors and Actuators B: Chemical*, vol. 48, no. 1-3, pp. 432–438, 1998.

[42] J. Jang and J. H. Oh, "Fabrication of a highly transparent conductive thin film from polypyrrole/poly(methyl methacrylate) core/shell nanospheres," *Advanced Functional Materials*, vol. 15, no. 3, pp. 494–502, 2005.

[43] P. Moozarm Nia, F. Lorestani, W. P. Meng, and Y. Alias, "A novel non-enzymatic H_2O_2 sensor based on polypyrrole nanofibers-silver nanoparticles decorated reduced graphene oxide nano composites," *Applied Surface Science*, vol. 332, pp. 648–656, 2015.

[44] G. Ruhi, O. P. Modi, and S. K. Dhawan, "Chitosan-polypyrrole-SiO_2 composite coatings with advanced anticorrosive properties," *Synthetic Metals*, vol. 200, pp. 24–39, 2015.

[45] F. S. Damos, R. C. S. Luz, and L. T. Kubota, "Investigations of ultrathin polypyrrole films: formation and effects of doping/-dedoping processes on its optical properties by electrochemical surface plasmon resonance (ESPR)," *Electrochimica Acta*, vol. 51, no. 7, pp. 1304–1312, 2006.

[46] M. R. Shishehbore, A. Afkhami, and H. Bagheri, "Salicylic acid functionalized silica-coated magnetite nanoparticles for solid phase extraction and preconcentration of some heavy metal ions from various real samples," *Chemistry Central Journal*, vol. 5, no. 1, pp. 1–10, 2011.

[47] A. R. Sadrolhosseini, A. S. M. Noor, A. Bahrami, H. N. Lim, Z. A. Talib, and M. A. Mahdi, "Application of polypyrrole multi-walled carbon nanotube composite layer for detection of mercury, lead and iron ions using surface plasmon resonance technique," *PLoS One*, vol. 9, no. 4, article e93962, 2014.

[48] S. Ebrahimiasl, A. Zakaria, A. Kassim, and S. N. Basri, "Novel conductive polypyrrole/zinc oxide/chitosan bionanocomposite: synthesis, characterization, antioxidant, and antibacterial activities," *International Journal of Nanomedicine*, vol. 10, pp. 217–227, 2014.

[49] I. Mironyuk, T. Tatarchuk, M. Naushad, H. Vasylyeva, and I. Mykytyn, "Highly efficient adsorption of strontium ions by carbonated mesoporous TiO_2," *Journal of Molecular Liquids*, vol. 285, pp. 742–753, 2019.

[50] I. Mironyuk, T. Tatarchuk, H. Vasylyeva, M. Naushad, and I. Mykytyn, "Adsorption of Sr(II) cations onto phosphated mesoporous titanium dioxide: mechanism, isotherm and kinetics studies," *Journal of Environmental Chemical Engineering*, vol. 7, no. 6, article 103430, 2019.

[51] S. Alvarez-Torrellas, M. Boutahala, N. Boukhalfa, and M. Munoz, "Effective adsorption of methylene blue dye onto magnetic nanocomposites. Modeling and reuse studies," *Applied Sciences*, vol. 9, no. 21, p. 4563, 2019.

[52] R. Nandini and B. Vishalakshi, "A study of interaction of methyl orange with some polycations," *E-Journal of Chemistry*, vol. 9, no. 1, pp. 1–14, 2012.

[53] E. Guibal, "Interactions of metal ions with chitosan-based sorbents: a review," *Separation and Purification Technology*, vol. 38, no. 1, pp. 43–74, 2004.

[54] O. A. C. Monteiro Jr. and C. Airoldi, "Some Thermodynamic Data on Copper-Chitin and Copper-Chitosan Biopolymer Interactions," *Journal of Colloid and Interface Science*, vol. 212, no. 2, pp. 212–219, 1999.

[55] K. Kofuji, Y. Murata, and S. Kawashima, "Sustained insulin release with biodegradation of chitosan gel beads prepared by copper ions," *International Journal of Pharmaceutics*, vol. 303, no. 1-2, pp. 95–103, 2005.

[56] F. Li, P. Du, W. Chen, and S. Zhang, "Preparation of silica-supported porous sorbent for heavy metal ions removal in wastewater treatment by organic–inorganic hybridization combined with sucrose and polyethylene glycol imprinting," *Analytica Chimica Acta*, vol. 585, no. 2, pp. 211–218, 2007.